Beam Test Results on Cluster Counting for IDEA Drift Chamber

Alessandro Corvaglia[1], Brunella D'Anzi [2,3], Nicola De Filippis [2,4*], Francesco De Santis [1], Walaa Elmetenawee [2*], Francesco Grancagnolo[1*], Edoardo Gorini[1], Alessandro Miccoli[1], Magdy Louka[2,3], Marco Panareo[1], Margherita Primavera[1], Francesco Procacci [2], Andrea Ventura[1]

[1]Istituto Nazionale di Fisica Nucleare Sezione di Lecce, Via Arnesano, 73100, Lecce, Italy.
[2] Istituto Nazionale di Fisica Nucleare Sezione di Bari, Via Giovanni Amendola, 173, 70126, Bari, Italy.
[3] Dipartimento di Fisica, Universit'a di Bari Aldo Moro, Via E. Orabona 4, 70126 Bari , Italy.
[4] Politecnico di Bari, Via E. Orabona 4, 70126 Bari , Italy.

*Corresponding author(s). E-mail(s): nicola.defilippis@ba.infn.it; walaa.elmetenawee@ba.infn.it; franco.grancagnolo@le.infn.it;
Contributing authors: alessandro.corvaglia@le.infn.it; brunella.danzi@ba.infn.it; francesco.desantis@le.infn.it; edoardo.gorini@le.infn.it; alessandro.miccoli@le.infn.it; magdy.louka@ba.infn.it; marco.panareo@le.infn.it; margherita.primavera@le.infn.it; f.procacci@phd.poliba.it; andrea.ventura@le.infn.it;

1 Introduction

In High Energy physics colliders, leveraging information on ionization energy loss (dE/dx) from charged particle tracks in gaseous detectors has been a traditional approach for particle identification (PID). Despite its utility, the effectiveness of this method is constrained by substantial uncertainties in total energy deposition, limiting

particle separation capabilities even in the most favorable momentum region (relativistic rise), where, the typical separation between energy loss curves related to different particles is often overshadowed by the spread around relative mean values [1].

To address these challenges, the cluster counting technique (dN/dx), which takes advantage of the Poisson nature of the primary ionization process has been introduced. This technique provides a more statistically significant means to infer mass information [1, 2]. Its efficacy stems from the independence of the number of primary ionizations from cluster size and gas gain fluctuations, as well as its insensitivity to highly ionizing γ-rays.

The cluster counting and the cluster timing techniques, originally proposed for the drift chamber of the KLOE experiment at the DAFNE facility of INFN in Frascati [3] and currently applied in the drift chamber of the MEG2 experiment at PSI [4], will be widely exploited in the INTREPID (INnovative Tracking detector Equipped with Particle IDentification), drift chamber proposed for the FCCee and CEPC facilities [5, 6].

2 The cluster counting technique: dN/dx

In Helium-based gas mixtures, the signals generated by ionization events in a gas detector can be spread in time on the order of a few nanoseconds. Utilizing fast read-out electronics facilitates efficient identification of these signals. By counting the number of ionization events per unit length (dN/dx), particles can be separated and identified with superior resolution compared to the conventional method based on ionization per unit length (dE/dx).

Analytical evaluations, reported in Figure 1, demonstrate that the cluster counting technique enhances particle separation capabilities by a factor of 2 compared to the dE/dx technique. The plot illustrates particle separation power in terms of standard deviations (sigma) as a function of momentum in a gas mixture of 90% He and 10% iC4H10. Solid curves represent separation using the cluster counting technique, while dashed curves depict the optimal energy loss truncated mean technique. The calculations assume an efficiency 80% for cluster counting. The technique exhibits excellent performance across the entire momentum range, experiencing only minor gaps in specific momentum intervals. Although these promising results warrant further investigation, a dedicated simulation campaign was conducted to confirm the potential of the technique.

3 Simulation of ionization clustering

To investigate the potential of the cluster counting technique, a reasonable simulation of the ionization cluster generation is needed [7]. Garfield++ [8] and Geant4 [9] are two valid software tools for the drift chamber simulations. However, Garfield++ can describe in detail the properties and the performance of a drift chamber single cell, but it is not suitable to simulate a large-scale detector and to study collider events. On the other side, Geant4 can simulate elementary particle interactions with the material of a complex detector and study collider events, but the fundamental properties and

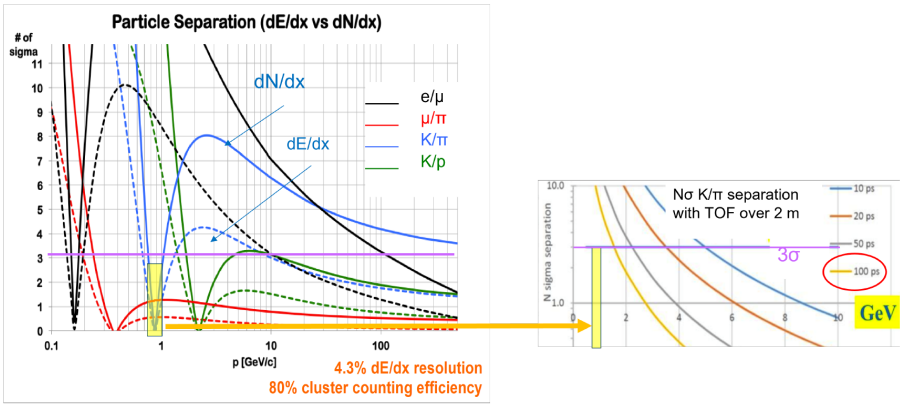

Fig. 1 Left: Analytic evaluation of particle separation capabilities achievable with dE/dx (solid curves) and dN/dx (dashed curves). The region between 0.85 GeV/c and 1.05 GeV/c where a different technique is needed is highlighted in yellow. Right: PID performance as a function of the time resolution by using a time of flight technique over 2 m to recover the particle identification around 1 GeV.

the performances of the sensible elements, like the drift cells, must be parameterized or "ad-hoc" physics models must be defined.

The goal has been to develop an algorithm, which could use the energy deposit information provided by Geant4, to reproduce, in a fast and convenient way, the number of clusters and the cluster size distributions predicted by Garfield++.

To this purpose, ionizing tracks crossing 200 drift cells, 1 cm wide, filled with a mixture of 90% He - 10% iC4H10 have been simulated with Garfield++. The resulting distribution of the number of clusters and of the energy loss for muons, pions, electrons, protons and kaons in a range of momentum from 100 MeV up to 100 GeV are reported in Figure 2.

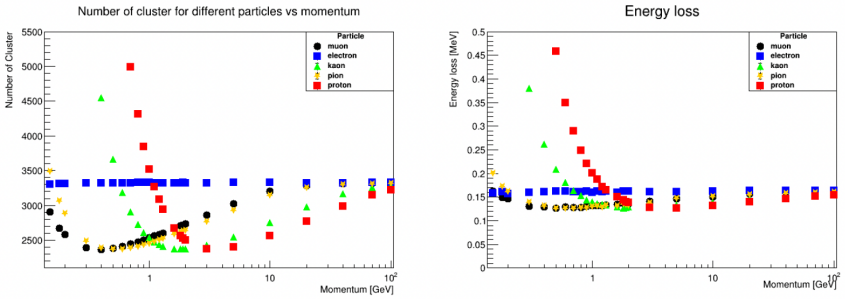

Fig. 2 Distribution of the number of clusters (left) and of the energy loss (right) for a 2 m long ionizing track.

Based on these distributions, the particle separation power has been calculated using the 70% truncated mean of the specific energy loss dE/dx and of the ionization cluster density dN/dx, as reported in Figure 3. It results clear that the cluster counting technique improves particle separation by a factor of 2 with respect to the traditional dE/dx method.

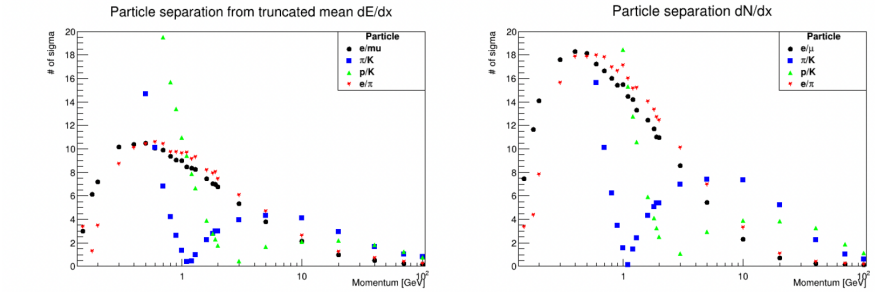

Fig. 3 Particle separation power with (70% truncated mean) dE/dx (left) and with dN/dx (right).

3.1 Evaluation of the modeled algorithm in Geant4 simulation

To efficiently study collider events, an attempt has been made to reproduce with Geant4 the same results obtained with the Garfield++ simulation. To this purpose, starting from the information provided by Geant4, different algorithms, modeling according to Garfield++ the ionization cluster kinetic energies containing a single electron and those containing more than one electron, have been implemented to reconstruct the distributions of the number of clusters and of the cluster size.

The algorithms have been validated by comparing their results to the ones simulated by Garfield++, in the case of 300 MeV/c muons crossing 200 drift cells, 1 cm wide, in 90% He - 10% iC4H10 gas mixture, as shown in Figure 4.

The algorithm successfully reproduces the expected distributions and has been validated for all particle types, over the full momentum range, providing consistent results in all cases. One can conclude that, starting from the energy loss distribution calculated by Geant4 - the energy loss is the only necessary information to be provided - and making use of the algorithms modeled by Garfield++, one can perform in the framework of Geant4 the same simulation as in Garfield++, avoiding the cumbersome task of following step by step the ionizing particle through the volume of a large detector.

3.2 Discrepancy between Garfield++ and Geant4 predictions

The particle separation, both in dE/dx and in dN/dx, as a function of the momentum for the different particle types, in the Garfield++ simulation and in the Garfield++

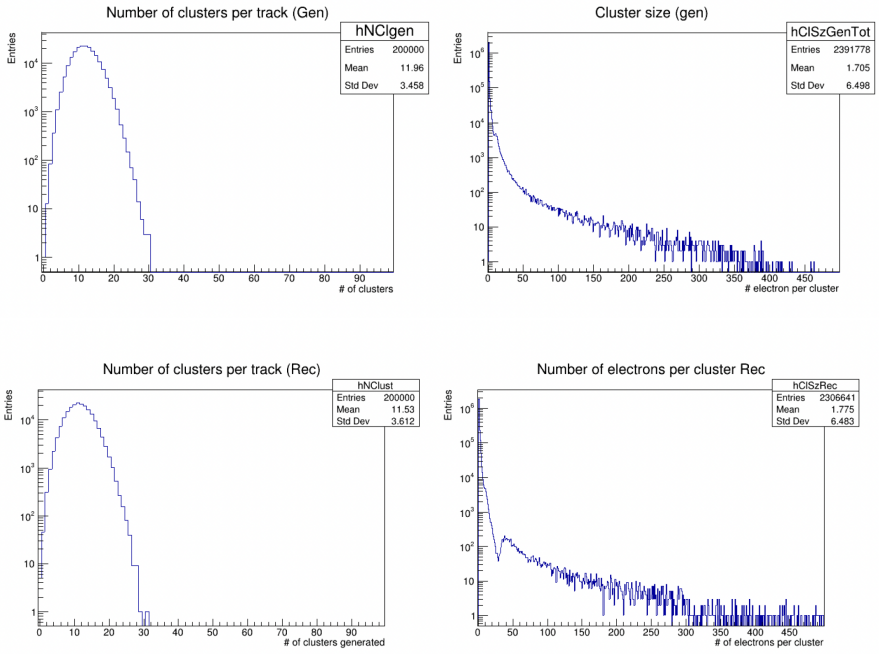

Fig. 4 Distributions of the number of clusters/cm (left) and of cluster size (right) for 300 MeV/c muons. Top plots: Garfield++ simulation. Bottom plots: modeled algorithm in Geant4 simulation.

modeled Geant4 simulation, is illustrated in Figure 5, indicating, however, a disagreement between the two frameworks despite the common Garfield++ model. Considering, as an example, the π/k separation at 5 GeV/c, one gets with the dE/dx method, from the Garfield++ simulation, a 50% better separation than what obtained from the Geant4 based simulation. Likewise, with the cluster counting method, one gets a 20% better performance. The motivation of such a discrepancy may reside in different cuts hardwired inside the two software. Indeed, the lack of experimental data on cluster density and cluster population for He based gas, particularly in the relativistic rise region, does not contribute to clarify these questions, which are crucial for establishing the particle identification performance at FCCee and CEPC.

Experimental measurements represent the ultimate way to shed light on these issues.

4 The beam tests

Besides providing a quantitative assessment of the particle identification performance, both with dE/dx and dN/dx, precise measurements at beam tests will allow to

- ascertain the Poisson nature of the cluster counting technique and its dependence on the $\beta\gamma$ of the ionizing track,

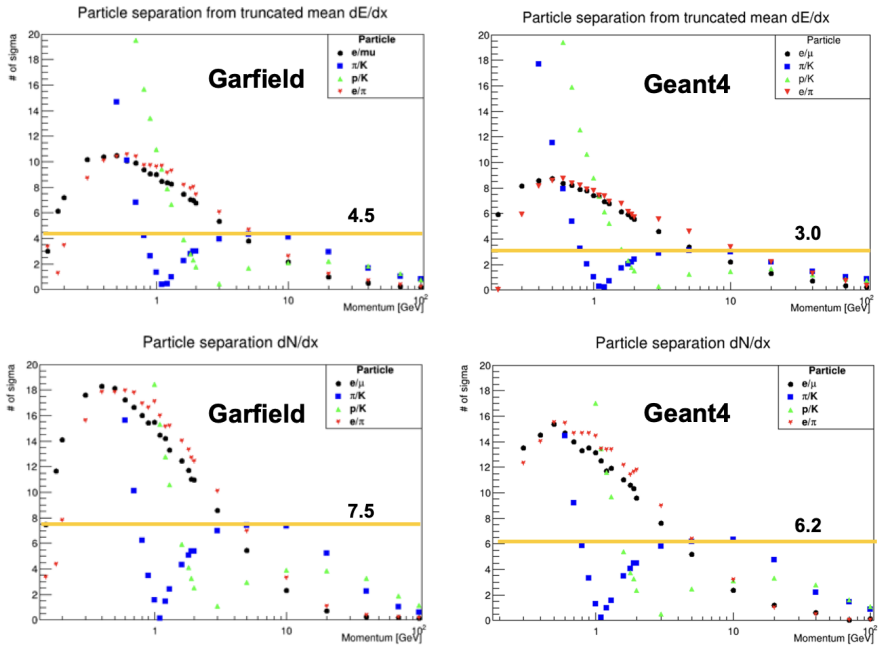

Fig. 5 Particle separations as a function of momentum with Garfield++ (at left) and Geant4 (at right). Top plots: separation in terms of dE/dx. Bottom plots: separation in terms of dN/dx

- establish the most effective cluster counting algorithms, in dependence of geometrical configuration, operative parameters like gas mixture, gas gain, electric field, frontend and digitizing electronics,
- define the limiting factors affecting an efficient cluster counting, like the cluster dimensions, the space charge distribution, the electron-ion recombination effects.

Different sets of square cross-section brass drift tubes, with sizes ranging from 1.0 to 3.0 cm, instrumented with different diameter sense wires, ranging from 10 to 40 μm, at different gas gains from 1 to 5 $\times 10^5$ and supplied with Helium-Isobutane gas mixtures in the ratios of 90/10, 85/15 and 80/20, were, therefore, placed in beams of muons of different momenta in three beam test campaigns over the last three years.

In November 2021 and July 2022, the beam test occurred at CERN in the SPS-H8 beamline with muons on the Fermi plateau from 40 to 180 GeV/c. In July 2023, the beam test occurred at CERN in the PS-T10 beamline with muons on the relativistic rise from 2 to 10 GeV/c. Figure 6 summarizes the beam test campaigns at CERN, together with some pioneering measurements done in a beam test at PSI many years ago.

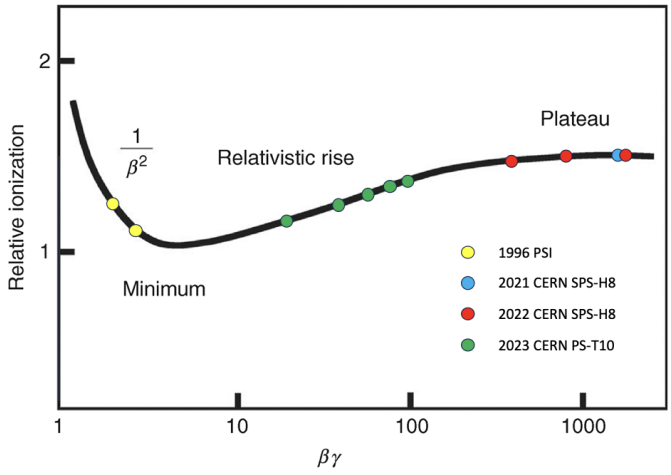

Fig. 6 Beam test campaigns with muons of the indicated $\beta\gamma$ values over imposed to a generic Bethe-Block curve. The explored $\beta\gamma$ values cover up the regions of interest for particle identification at the future lepton colliders.

4.1 The experimental setup

Figure 7 is a picture taken upstream of the beamline and shows all details of the drift tubes (hidden by the copper tape shielding) setup with the rest of the experimental apparatus for the 2021 beam test. Analogous setups were arranged for the subsequent beam tests.

The drift tubes sense wires were connected on one end to a HV supply card and, on the other end to a HV decoupling termination card, with 330 Ω (average impedance among the different tube sizes and sense wire diameters) directly connected – no preamplifier was used despite the long 40 cm (60 cm in the 2023 beam test) coaxial cables, – to the readout system. The trigger signal was provided by a coincidence of scintillators readout by SiPM. The gas mixture was provided by mass flowmeters at ambient NTP conditions.

The readout system was provided by the Wave Dream Board (WDB) [10], shown in Figure 8, developed at PSI for the MEG2 experiment [4]. It contains 16 channels with variable gain amplification and flexible shaping through a programmable pole-zero cancellation. Shaping and pole-zero cancellation have not been used throughout the beam tests.

Two DRS4 chips are connected to two 8-channel ADCs, which are read out by a Field-Programmable Gate Array (FPGA). In normal operation, the DRS4 chips work in "transparent mode", where the input signals are continuously sampled at a speed up to 5 GSPS in an analogue ring buffer. At the same time, a copy of the input signal is sent to the DRS4 output, where it is digitized by the ADCs at 80 MSPS with a resolution of 12 bits. The output stream of the ADCs is used in the FPGA to perform complex trigger algorithms such as a threshold cut on the sum of all input channels.

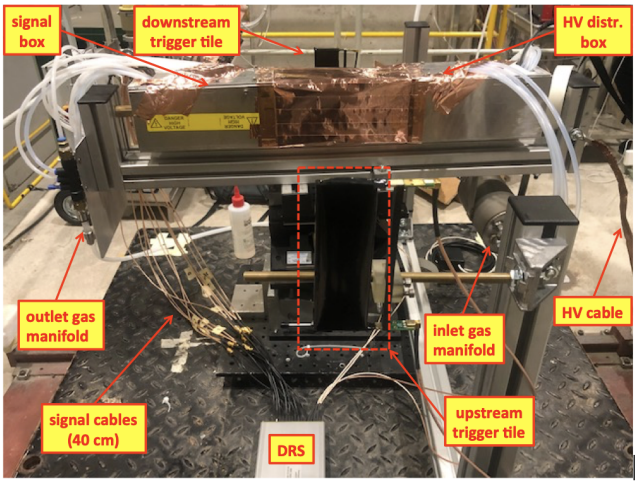

Fig. 7 The experimental setup seen from the beam upstream. The main components of the setup are indicated by the yellow insets

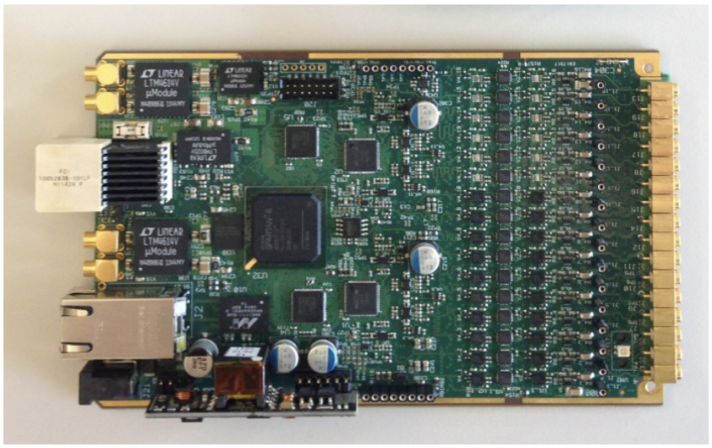

Fig. 8 The Wave Dream Board.

The WDB can be used in stand-alone mode, where it is read out through Gigabit Ethernet. An ultra-low noise bias voltage generator is also implemented in the WDB to power up, through the signal cables, the SiPMs defining the trigger.

The advantages of such a setup are several:

- one can use only muon beams at different $\beta\gamma$ values to explore the particle identification over the full range of momenta,

- one can use thick metal tubes piled one after the other since multiple scattering is irrelevant for path length differences,
- it does not require external tracking to define the drift path length: it is sufficient to consider constant the path length inside the drift tube active volume,
- it does not require internal tracking (no need for t_0 calibrations, alignment, time to distance conversion): one just counts clusters in the time domain.

Figure 9 shows the display of one event acquired with the WDB. Its interface acts in analogy to an oscilloscope, as can be seen from the left side of Figure 9 The first four channels represent the trigger scintillators (upstream and downstream of the drift tube setup), readout by SiPMs powered up by the WDB. The trigger (coincidence of the 4 channels) is generated internally by the WDB. The successive 6 channels are the signal on a row of 1 cm drift tubes, hit by the same muon.

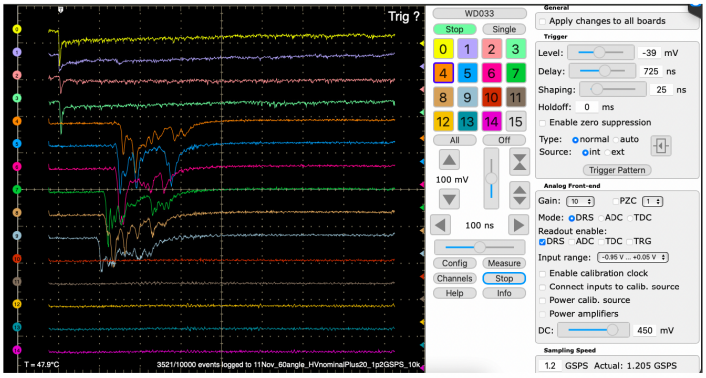

Fig. 9 The event display of the Wave Dream Board. On the right side, the control panel of the WDB for the channel setup (gain, threshold, bias voltage, sampling rate, etc.) and for accessing the trigger definition panel.

The events, written in binary format, out of the WDB are then converted in Root format and shown, as examples, in Figure 10 for the data collected in 2021. The first row of four channels represents the trigger scintillator signals in all three events. In the left plot one can see a muon passing through a row of 6 drift tubes, 1 cm wide. In the central plot, a muon passing through a row of 3 drift tubes, 2 cm wide. In the right plot, a muon passing through a row of 2 drift tubes, 3 cm wide. The full vertical scale is 300 mV, and the horizontal scale is 900 ns. All channels are amplified by a factor 10 within the WDB.

5 Results

The definition of the operating parameters of the various drift tubes under different conditions, in particular the gas gain, which determines the single electron pulse height,

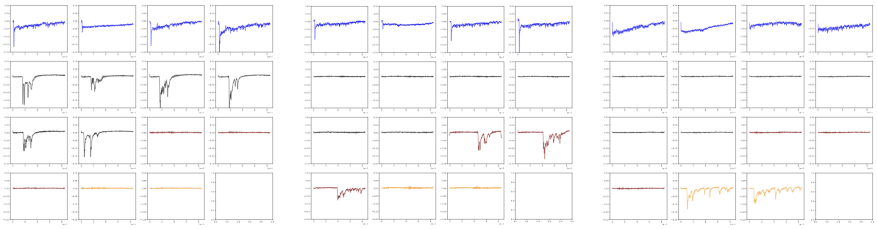

Fig. 10 Three events converted in Root format.

represents the preliminary step for a homogeneous data collection when studying, for example, the efficiency of the different cluster counting algorithms.

5.1 Gas gain test

The gas gain as a function of the anode HV has been calculated by fitting with a Landau distribution the single electron pulse height (Figure 11) and correcting the fitted MPV for the amplifier gain, for the impedance mismatch between the characteristic tube impedance and the 330 Ω termination resistor and for the current divider between the 330 Ω termination resistor and the 50 Ω input impedance of the ADC.

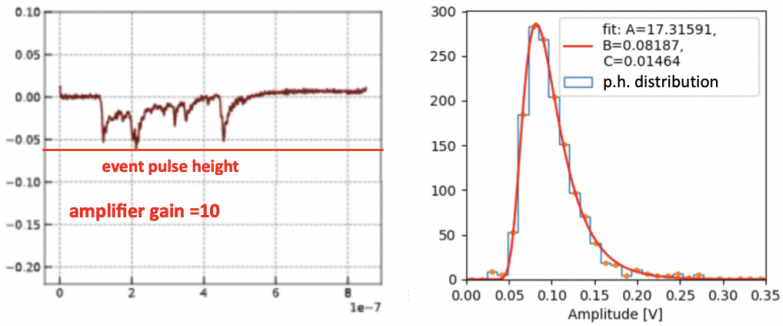

Fig. 11 Right: the Landau fit to the distribution of the pulse height (at left). The MPV value (parameter B in the inset) is then used for the calculation of the gas gain.

In Figure 12 the gas gain is plotted as a function of the anode high voltage for all drift tubes configurations - 2021 beam test, 90% He-10% iC4H10 gas mixture at 725 torr absolute pressure, data collected at normal beam incidence to the sense wires. Figure 13 shows the analogous plot for the 2022 beam test with different size drift tubes and different gas mixtures.

It is clear from these data that, for an effective exploitation of the cluster counting techniques, the range of gas gain, independently of the drift tube configuration (drift length, sense wire diameter, gas mixture), lies within 1×10^5 and 5×10^5.

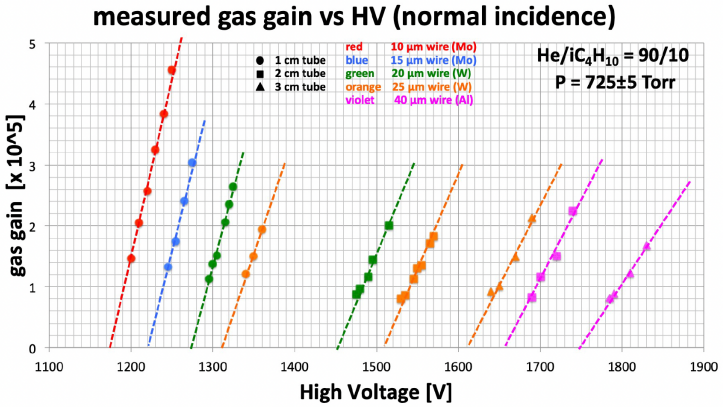

Fig. 12 Gas gain as a function of the anode high voltage based on November 2021 test beam data. The gas mixture and the absolute gas operating pressure are indicated. Different size drift tubes are represented by distinct symbols, while various sense wire diameters are indicated by different colors. The dashed lines are only to guide the eye.

5.2 Avalanche size

The single electron avalanches overlap as a function of the angle α between the track direction and the normal to the sense wire (see Figure **??**) has been studied to estimate the size of the amplification avalanche and its effects on the extension of the space charge around the sense wire.

Space charge effects, at any given angle, result in modifying the effective gas gain (or, equivalently, the average single electron pulse height). For 165 GeV/c muons (2021 beam test) and 90% He - 10% iC4H10 gas mixture, the expected number of cluster is N $\approx$ 16.5/cm with an average separation λ between consecutive clusters of 600 μm. Figure 14 shows the avalanche separation, λ sinα, projected on the sense wire.

Figure 15 shows at left a plot of the average single electron pulse height as a function of the avalanche separation, λ sinα, on a 2 cm drift tube instrumented with 20 μm sense wire for different gas gains. The plot suggests no strong dependence of space charge effects from the gas gain, at least in this range of gas gain values. Figure 15 at right, shows the same quantity for different sense wire diameters at approximately equal gas gains for the 1 cm drift tubes. It suggests no strong dependence of space charge effects from the sense wire diameter, at least for this gas gain value.

From these data one can conclude that, for 90% He - 10% iC4H10 gas mixture and a few $\times 10^5$ gas gain, the effect of space charge results, for normal track incidence to the sense wire ($\alpha = 0^0$), in approximately 70% avalanche suppression. A naive model based on isotropic spherical avalanches gives, for these configurations, a radius r_{av} of approximately 450 μm. The condition of no avalanche overlap: λ sin$\alpha \geq 2r_{av}$is met for $1/\lambda$ = N $\leq$ 11/cm. Any helium/isobutane gas mixture richer than 10% isobutane

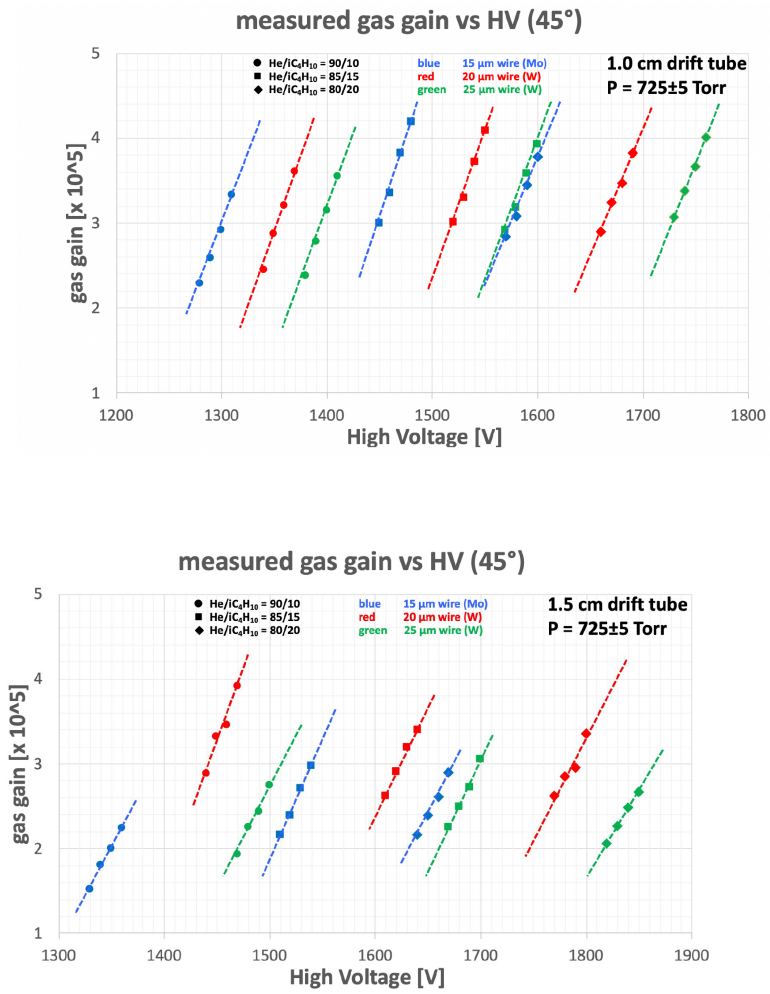

Fig. 13 Gas gain gain as a function of the anode high voltage based on July 2022 test beam data for cell drift tubes with 1 cm (top) and 1.5 cm (bottom) dimensions. The 45° angle refers to the angle between the beam direction and the normal to the sense wire. The absolute gas operating pressure are indicated. Different gas mixtures are represented by distinct symbols, while various sense wire diameters are indicated by different colors. The dashed lines are only to guide the eye.

(corresponding to N $\geq$ 12/cm for a m.i.p.) will, therefore, necessitates space charge effects corrections for an efficient application of the cluster counting techniques.

5.3 Electron Peak Finding

The results presented in this paper were obtained using two distinct methods for electron peak-finding. Prior to their application, a preprocessing step was employed

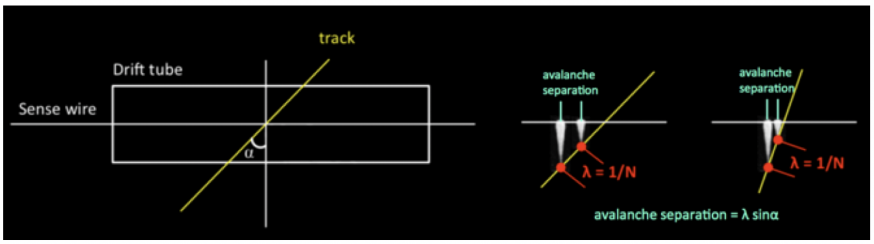

Fig. 14 Space charge effects depend on the angle α between the track direction and the normal to sense wire orientation. The avalanche separation projected on the sense wire, λ sinα, is indicated.

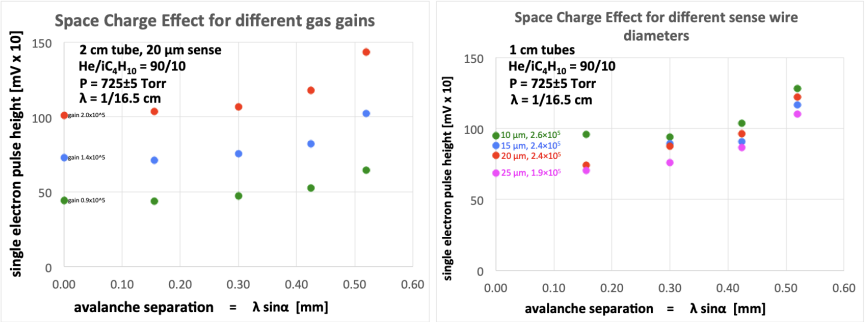

Fig. 15 Left: Single electron pulse height as a function of the projected avalanche separation for different gas gains in the 2 cm drift tube instrumented with a 20 μm sense wire. Right: Single electron pulse height as a function of the projected avalanche separation for different sense wire diameters at approximately equal gas gain in the 1 cm drift tube.

on the data collected during beam tests to establish the waveform baseline at zero. In this process, we defined and subtracted the root mean square (r.m.s.) error from each waveform by averaging over its initial 30 ns, a period dominated by noise effects.

The first employed technique is a second derivative-based (DERIV) algorithm. This method calculates the first and second derivatives by determining the ratio between amplitude averages over two consecutive bins and twice their bin size, dependent on the sampling rate. Subsequently, it mandates that at the position of the peak candidate, the derivatives are less than a scanned quantity proportional to the waveform r.m.s. (ϵ), and they must increase (decrease) before (after) the peak candidate position by an ϵ-based small quantity. The algorithm also imposes lower limit boundaries based on r.m.s. on the amplitude at peak candidate positions and on the voltage difference between the peak candidate amplitudes and the previous (next) bin ones.

The second methodology used for peak finding is the Running Template Algorithm (RTA). This approach defines an electron pulse template with raising (K_{rise}) and falling (K_{fall}) exponentials over a fixed number of bins (K_{tot}) and digitized (A (k)) to replicate the behavior of the data, as shown in Figure 16. The algorithm scans the waveform, progressing over the K_{tot} bins window by comparing the electron pulse shape to the normalized data. It constructs an agreement assessment quantity (χ^2)

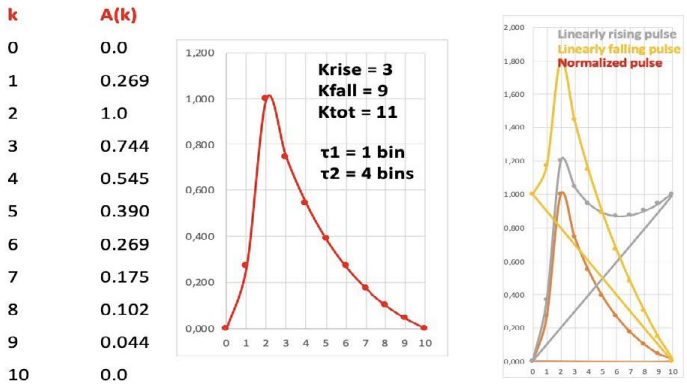

Fig. 16 Example of an electron template pulse used to scan the waveforms by the RTA algorithm.

and establishes a cut-off. RTA subtracts the identified peak from the signal spectrum and iterates the search until no new peaks are found.

An illustration of the peaks identified by the two aforementioned algorithms is presented in Figure 17 for 1 cm drift tubes. In addition, the distributions of the number of peaks have been studied. An example of the number of peaks founded by the two algorithms is reported in Figure 18, where the number of electrons founded by the algorithm is compatible with the one expected according to the physics of the process.

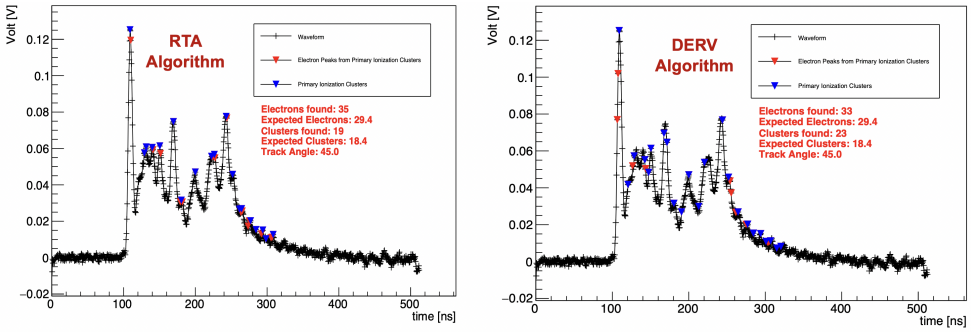

Fig. 17 Data waveform recorded for a 1 cm drift cell with a 20 μm sense wire diameter, a 45° track angle, a sampling rate of 2 GSa/s, and a He/iC_4H_{10} 90/10 gas mixture. The RTA algorithm (left) and DERIV algorithm (right) are used for electron peak identification, with cluster peaks indicated by blue arrows and electron peaks by red arrows.

5.4 Clusterization

The process of identifying primary ionization clusters, referred to as "clusterization," involves the proper association of electron peaks identified by the algorithms described in Section 5.3. It aims to define a time position and amplitude for each cluster. Initially,

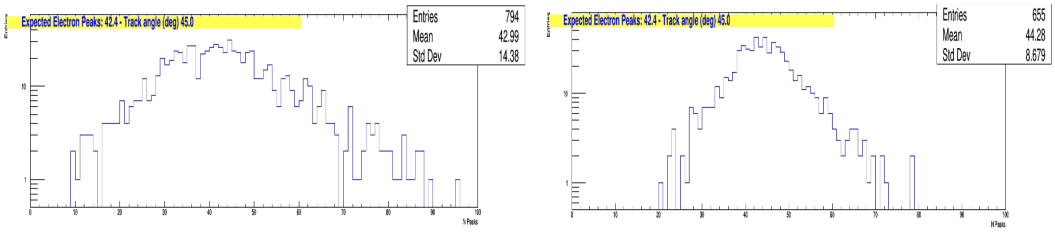

Fig. 18 Distribution of the number of peaks for a 1 cm drift cell, 15 μm sense wire diameter, 45° track angle, sampling rate of 2 GSa/s and gas mixture He/iC4H10 80/20 by applying the DERV algorithm (on the left) and RTA algorithm (on the right).

the algorithm merges consecutive electron peaks into a single entity to reduce the potential of fake electrons.

Subsequently, contiguous electron peaks which are compatible with the electrons' diffusion time are associated to the same ionization cluster. An electron count per cluster is incremented for these peaks. The clusterization algorithm considers the dependence of electrons' diffusion time on the electron arrival time, approximately proportional to the square root of the electron time arrival, as well as on the gas mixture utilized (e.g., experiencing a 20% drift velocity change transitioning from He:IsoB 90/10 to 80/20).

Ultimately, the position and amplitude of the clusters correspond to those of the electrons with the highest amplitude within the cluster. An illustration of the peaks identified by the two aforementioned algorithms in one waveform is presented in Figure 17 for 1 cm drift tubes and Figure **??** for 1.5 cm drift tubes.

Figure 19 and Figure 20 illustrate the distribution of clusters and the respective count of electrons per cluster as determined by the clusterization algorithm. The red line overlaid on the plots in Figure 19 represents the result of a Gaussian fit, the mean being consistent with the expected value.

5.5 RTA templates scan

Figure 21 showcases different templates utilized within the RTA algorithm for the identification of electron peaks. Each template shows variations in the rising and falling times.

5.6 Comparison of the DERV and RTA algorithms

5.7 Performance scans

Using test beam data, we evaluated the performance of our algorithms across a range of operational conditions, including gas mixtures, gain, geometrical configurations (such

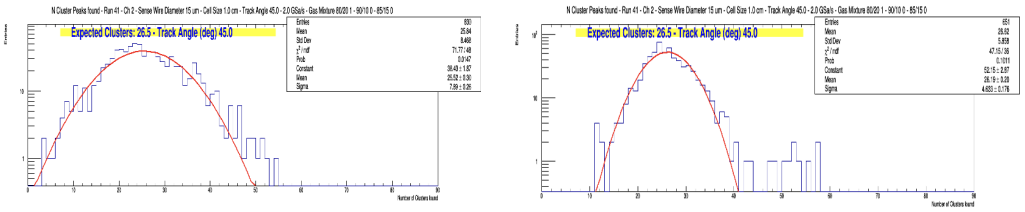

Fig. 19 Distribution of the number of clusters for a 1 cm drift cell, 15 μm sense wire diameter, 45° track angle, sampling rate of 2 GSa/s and gas mixture He/iC4H10 80/20 by applying the DERV + clusterization algorithm (on the left) and RTA + clusterization algorithm (on the right).

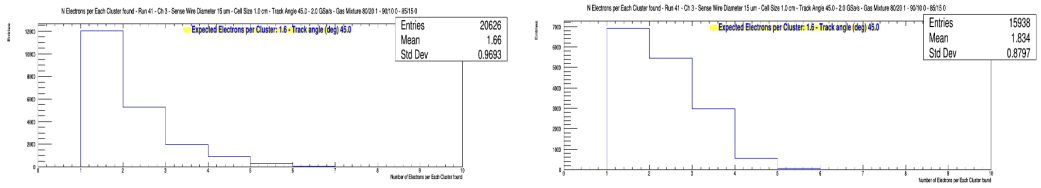

Fig. 20 Distribution of the number of electrons per cluster for a 1 cm drift cell, 15 μm sense wire diameter, 45° track angle, sampling rate of 2 GSa/s and gas mixture He/iC4H10 80/20 by applying the DERV + clusterization algorithm (on the left) and RTA + clusterization algorithm (on the right).

as cell size and sense wire dimensions), sampling rate, high voltage (HV), and track angle. This section presents scans of cluster counting efficiency, providing key insights into how various parameters—gas gain, angle, and gas composition—impact the drift chamber's ability to detect ionization clusters.

To account for differences in drift velocities across different gas mixtures, the clusterization cuts are optimized individually for each mixture. Figure 23 (left) displays the efficiency of the cluster counting for the three different helium-isobutane gas mixtures: 90/10, 85/15, and 80/20. The results are consistent with the expected specific ionizations, producing approximately 12, 15, and 18 clusters per cm per minimum ionizing particle (m.i.p.), respectively.

Additionally, we examined how the number of clusters scales with track length by comparing results at varying beam angles. Figure 23 (middle) presents the ratio of counted clusters to expected clusters as a function of beam angle for two gas mixtures. The observed cluster deficit at normal incidence for the 80/20 gas mixture is likely due to space charge effects, while at large angles, the higher ionization electron densities affect the efficiency of the cluster counting algorithms.

Figure 23 (right) shows the relationship between counting efficiency and gas gain, with each step in the HV configuration corresponding to approximately a 20% variation

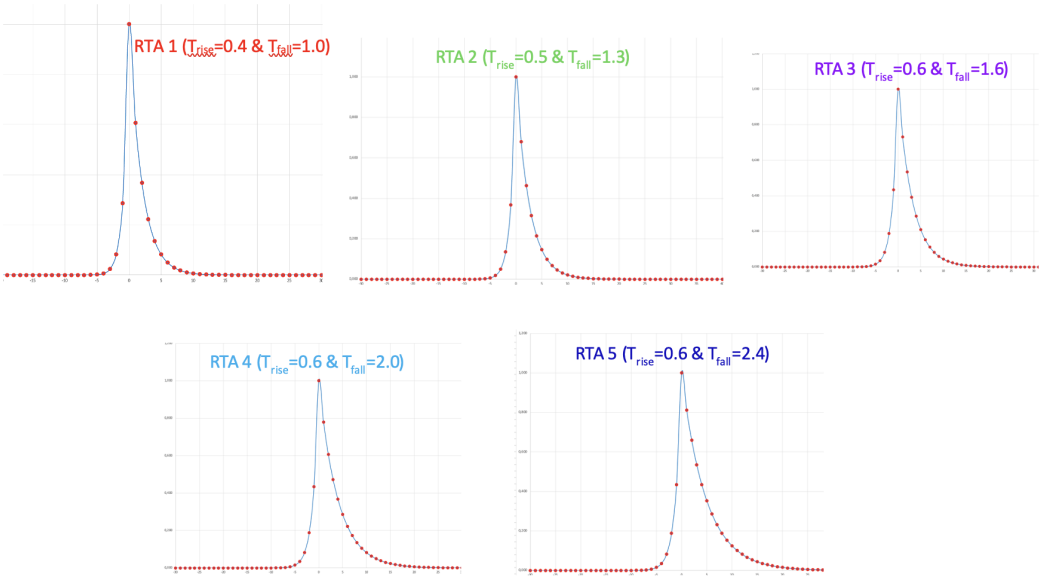

Fig. 21 Different templates of the RTA algorithm that used for identifying electron peaks, featuring adjustments in both rising and falling times.

in gain. A slight dependence of counting efficiency on gas gain is observed, highlighting the sensitivity of the detection process to gain variations. It is worth to mention that all peak finding parameters used for this analysis are optimized for the HV configuration 0 and undercounting and overcounting can be corrected by slight modifications of these parameters.

5.8 Resolution study

This section presents a comparative analysis of the resolution obtained from the measurement of charge deposits along a particle's track (dE/dx) and the ionization clusters (dN/dx), using identical tracks made of the same hits for both methods.

The measurement of energy loss along a particle's track, dE/dx, follows a Landau distribution as shown in Figure 25, characterized by a long tail caused by high-energy δ electrons. To calculate the energy loss, the charge deposited in multiple drift cells along the track is recorded, and the mean charge of these samples is taken as the dE/dx value. However, this simple mean is sensitive to large fluctuations due to the nature of the Landau distribution, where outliers with high charge deposits can skew the result. To address this, the truncated mean method is employed, discarding the highest charge samples—typically the top 20-30%—and calculating the mean of the remaining samples. The truncation threshold is empirically optimized to achieve the

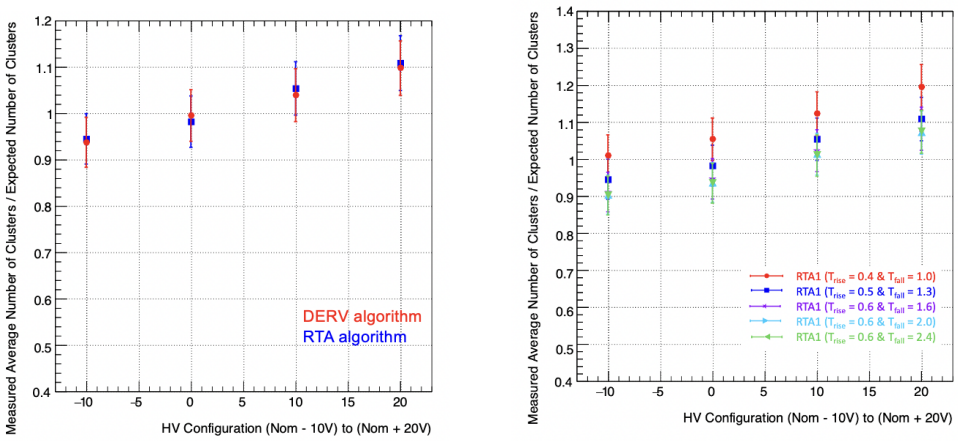

Fig. 22

best dE/dx resolution, with the optimal configuration retaining 80% of the charge distribution.

The resolution of dN/dx is estimated using the same tracks employed for the dE/dx analysis. The RTA + clusterization algorithm, as described above, is applied to reconstruct the ionization clusters. The truncated charge distribution was then compared with the number of ionization clusters measured along a 2-meter track length, as shown in Figure 26. The results demonstrate that the dN/dx method achieves a resolution of 3%, which is nearly twice as good as the 5.7% resolution obtained from the dE/dx method, in agreement with both analytical calculations and simulation predictions.

Furthermore, the resolution is evaluated for different track lengths, as shown in Figure 27, for both the dE/dx and dN/dx methods. The resolution dependence on track length is found to follow the $L^{-0.37}$ scaling for dE/dx, consistent with the Lehraus plot [**?**], and the $L^{-0.5}$ scaling for dN/dx, highlighting the superior resolution offered by the cluster counting technique.

6 Conclusions

The cluster counting technique has demonstrated significant potential for improving particle identification capabilities, as confirmed by both analytical evaluations and simulations. Two key algorithms, DERV and RTA, are developed to detect electron peaks and delivered results closely aligned with expectations. The performance of these algorithms is evaluated using test beam data under various conditions. A resolution study confirmed that the dN/dx method achieved resolution twice as good as that of the traditional dE/dx method, consistent with theoretical predictions. Further insights, particularly in the relativistic rise region, are anticipated from the upcoming 2024 test beam results.

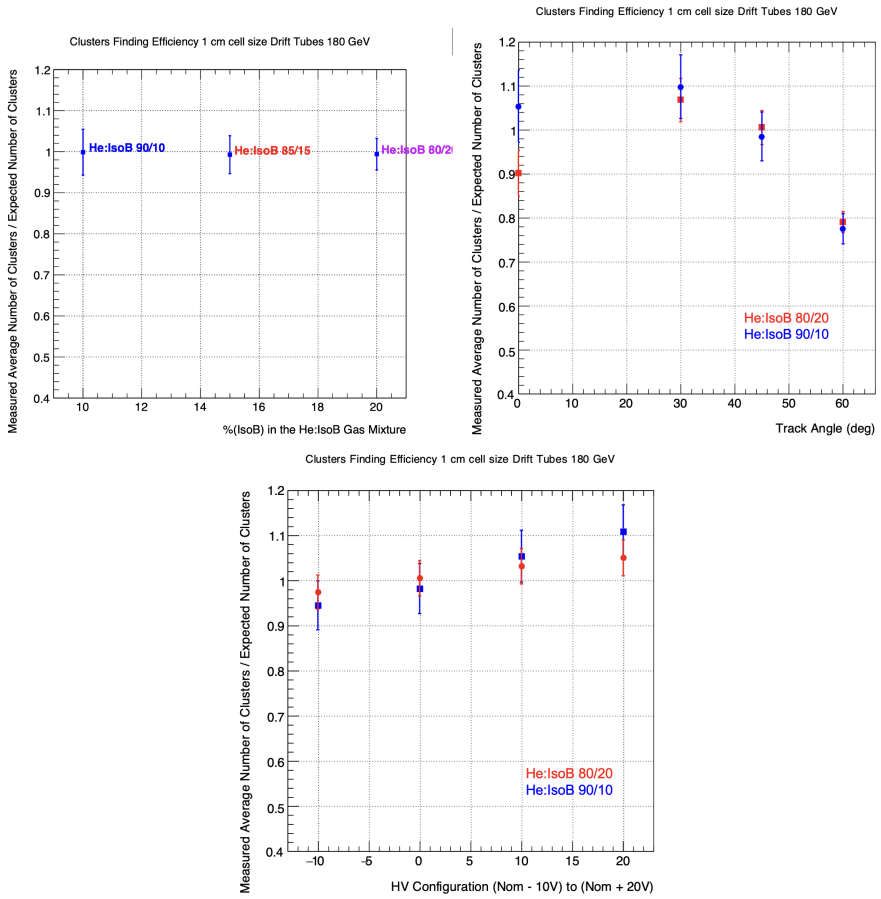

Fig. 23 Comparison plots showing the cluster counting efficiency as a function of gas mixture (left), track angle (middle), and drift tube high voltage settings (right) using the RTA + clusterization algorithm.

References

[1] G. Cataldi, F. Grancagnolo, S. Spagnolo, Cluster counting in helium based gas mixtures. Nuclear Instruments and Methods in Physics Research **386**(2), 458–469 (1997). https://doi.org/https://doi.org/10.1016/S0168-9002(96)01164-3

[2] C. Lippmann, Particle identification. Nuclear Instruments and Methods in Physics Research **666**, 148–172 (2012). https://doi.org/https://doi.org/10.1016/j.nima.2011.03.009

[3] F. Cataldi, G. Grancagnolo, S. Spagnolo, Cluster counting in helium-based gas mixtures. Nucl. Instrum. Meth. **386**, 458–469 (1997)

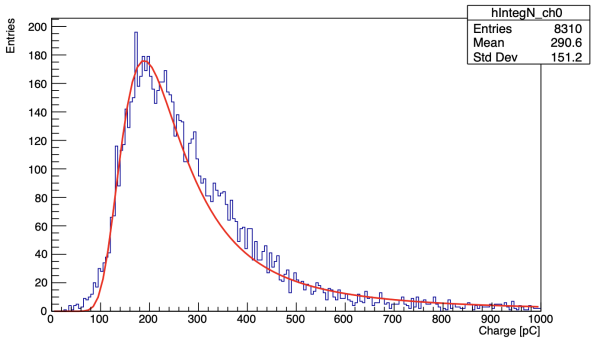

Fig. 24 The integral charge distribution

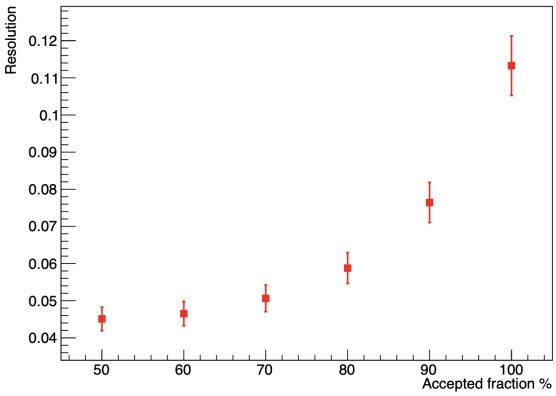

Fig. 25 Resolution for the dE/dx method as a function of the fraction of the truncated mean charge distribution

[4] A. Baldini, et al., The ultra-light drift chamber of the meg2 experiment. Nucl. Instrum. Meth. **A 958**, 162152 (2020)

[5] M. Benedikt, et al, The lepton collider: Future circular collider conceptual. Eur. Phys. J. Spec. Top.228 **386**(2), 261–623 (2019)

[6] W. Elmetenawee, et al, The Tracking performance for the IDEA drift chamber. PoS **ICHEP2022**, 362 (2022). https://doi.org/10.22323/1.414.0362

[7] F. Cuna, N. De Filippis, F. Grancagnolo, G. Tassielli, Simulation of particle identification with the cluster counting technique (2021)

[8] Https://garfieldpp.web.cern.ch/garfieldpp/

[9] URL https://geant4.web.cern.ch/node/1

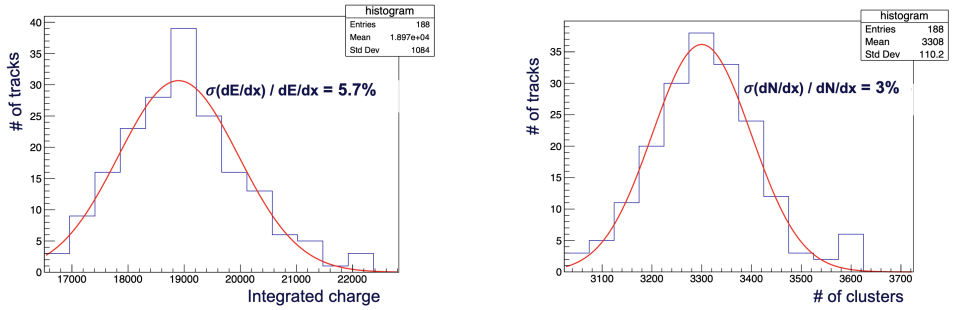

Fig. 26 The integral of the truncated mean charge distribution at 80% (left) and the number of ionization clusters (right) measured along 2-meter tracks made of the same hits. The red lines superimposed on the plots represent the result of Gaussian fit.

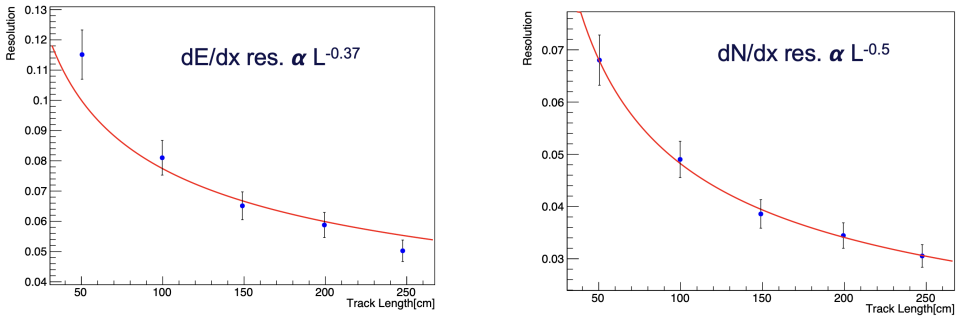

Fig. 27 Resolution as a function of track length (L) for the dE/dx method (left) and dN/dx method (right). The red lines superimposed on the plots show the fits of $L^{-0.37}$ for dE/dx and $L^{-0.5}$ for dN/dx.

[10] S. Ritt, R. Dinapoli, U. Hartmann, Application of the drs chip for fast waveform digitizing. Nuclear Instruments and Methods in Physics Research Section A: Accelerators, Spectrometers, Detectors and Associated Equipment **623**(1), 486–488 (2010). https://doi.org/https://doi.org/10.1016/j.nima.2010.03.045. URL https://www.sciencedirect.com/science/article/pii/S0168900210006091. 1st International Conference on Technology and Instrumentation in Particle Physics